Contents lists available at ScienceDirect

Chinese Chemical Letters

journal homepage: www.elsevier.com/locate/cclet

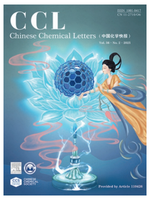

Green innovation unleashed: Harnessing tungsten-based nanomaterials for catalyzing solar-driven carbon dioxide conversion

Weidan Meng[a,b], Yanbo Zhou[a,d], Yi Zhou[a,b,c,d,*]

[a] *State Environmental Protection Key Laboratory of Environmental Risk Assessment and Control on Chemical Process, East China University of Science and Technology, Shanghai 200237, China*
[b] *National Engineering Research Center of Industrial Wastewater Detoxication and Resource Recovery, East China University of Science and Technology, Shanghai 200237, China*
[c] *Shanghai Engineering Research Center for Multi-media Environmental Catalysis and Resource Utilization, East China University of Science and Technology, Shanghai 200237, China*
[d] *Shanghai Institute of Pollution Control and Ecological Security, Shanghai 200092, China*

ARTICLE INFO

Article history:
Received 1 January 2024
Revised 8 April 2024
Accepted 30 April 2024
Available online 1 May 2024

Keywords:
Carbon dioxide photoreduction
Tungsten-based nanocatalyst
Mechanism
Performance evaluation
Selectivity

ABSTRACT

Carbon dioxide photocatalytic reduction (CO_2-PR) is an efficient method for controlling CO_2 emissions and generating cleaner energy while mitigating global warming. Tungsten oxides (W_xO_y) have attracted considerable attention for CO_2-PR due to their excellent spectral absorbance. However, comprehensive reviews are lacking on the use of W_xO_y for CO_2-PR. Therefore, this review provides a detailed summary of t research progress made with W_xO_y-based catalysts in CO_2-PR. It also explains the fundamental principles of CO_2-PR and evaluates key performance indicators that affect the activity of W_xO_y-based photocatalysts, including yield, selectivity, stability, and apparent quantum yield. Additionally, this review explores opportunities for synthesizing high-performance W_xO_y-based photocatalysts and highlights their potential for the green preparation of C1/C2 products through CO_2-PR. These innovative strategies aim to address the challenges and pressures associated with energy and environmental issues, particularly by enhancing artificial photosynthesis efficiency.

1. Introduction

The worldwide demand for energy is expected to continue increasing in the coming decades. The extensive burning of fossil fuels over the past centuries has resulted in the release of substantial amounts of greenhouse gases, which has aggravated global warming and the ecological crisis. It is projected that by the end of the 21st century, the anthropogenic CO_2 levels will reach 950 ppm [1]. If atmospheric CO_2 concentrations surpass 600 ppm, it will cause a devastating catastrophe for the earth, with a sea level rise of 0.4 m. Numerous technologies, such as carbon storage, carbon capture, and carbon utilization have been developed to reduce atmospheric CO_2 concentrations. Converting CO_2 into high-value-added chemicals, such as fuels or other manufactured products, has emerged as a promising solution to combat global warming and the energy crisis [2,3]. Photocatalytic technology has been extensively employed for the treatment of pollutants in water or air, and has demonstrated significant efficacy in the degradation of emerging pollutants [4-7]. This precisely utilizes visible light to induce the production of more active substances, which facilitates the separation of photogenerated carriers for the removal of pollutants [8,9]. Carbon dioxide photocatalytic reduction (CO_2-PR) technology, relying on economical reactants (*e.g.*, H_2O) and low energy requirements, has been recognized as a prospective approach to alleviate the energy crisis and global warming problem [10,11].

Tungsten oxide-based (W_xO_y-based) materials have garnered significant attention in CO_2-PR research. Typical W_xO_y materials, such as non-stoichiometric $W_{18}O_{49}$ and $WO_3 \cdot H_2O$, possess abundant defect sites that contain an excess of electrons compared to other defective semiconductors. These photocatalysts exhibit the localized surface plasmon resonance (LSPR) effect, which involves exciting the excess electrons [12]. The LSPR effect in WO_{3-x} extends its photoresponse to the near-infrared range, thereby enhancing the photoconversion efficiency and charge separation efficiency [13]. As a result, W_xO_y-based materials are able to exhibit excellent catalytic performance in CO_2-PR. However, photocatalysts are often unable to effectively realize the photoconversion of CO_2 because of the limitations of their own structures and proper-

---

[*] Corresponding author.
E-mail address: yizhou@ecust.edu.cn (Y. Zhou).

https://doi.org/10.1016/j.cclet.2024.109961

ties. Scientists have proposed diverse methods, such as defect engineering [14], structure control [15], morphology control [16], and the introduction of other metals or metal oxides to construct composite semiconductors and boost photocatalytic activity.

While few reviews have delved into the improvement of CO_2-PR performance through modification of W_xO_y-based catalysts, this paper aims to review recent research progress in this field. Specifically, we focus on different product perspectives, analyze and compare the influencing factors of CO_2-PR activity based on variations in photocatalytic systems across different studies, summarize and forecast the application of W_xO_y-based catalysts in the realm of CO_2-PR. We firmly believe that this review will facilitate future design and study of CO_2-PR, as well as encourage further exploration of W_xO_y-based photocatalytic systems for a wide range of applications.

2. Basic principle of CO_2-PR

2.1. Models of CO_2 adsorption and activation on photocatalysts

CO_2 is thermodynamically stable due to its centrosymmetric linear molecular structure and fully oxidized chemical state ($\Delta H_f^0 = -393.51$ kJ/mol), characterized by an O=C=O linear structure with σ and π bonds [17]. The bond energy of C=O (750 kJ/mol) is significantly higher than that of C–O (327 kJ/mol), C–H (411 kJ/mol), and C–C (336 kJ/mol) bonds [18]. CO_2-PR is a highly endothermic process with an energy barrier that must be overcome to cleave the C=O bond and excite CO_2-PR.

In the original CO_2 adsorption activation theory, an ideal model was proposed based on metal/metal oxide photocatalysts (Figs. S1a and b in Supporting information) [19,20]. Typically, photocatalysts possessing mesoporous structures offer larger surface areas and pore volumes, thereby facilitating an increased number of active sites for CO_2 adsorption [21,22]. Moreover, CO_2 functions as an acidic oxide, and its carbon atoms, acting as Lewis acids, can coordinate with Lewis base sites on the photocatalyst surface, which are represented by oxygen atoms acting as Lewis bases [23]. This coordination results in the distortion of CO_2's linear structure and consequent generation of partially charged $CO_2\ \delta^-$ species [19]. Throughout the structural transformation from linear to bent conformation, the lowest unoccupied molecular orbital (LUMO) of the CO_2 molecule is downshifted, thereby promoting charge transfer between the catalyst and $CO_2^{\bullet-}$ species [24].

The CO_2-PR pathway and its product selectivity depend strongly on the surface chemistry of CO_2 adsorption on the surface of the photo-/co-catalyst and desorption of the intermediates, which has been comprehensively summarized in other reviews (Fig. S1c in Supporting information). The crucial step in the reaction is the activation of the first C–O bond within the CO_2 molecule, and efficient electron transfer to CO_2 facilitates its activation [25,26]. It has been extensively shown that incorporating catalytically active sites comprising metals and oxides facilitates CO_2 activation and the stabilization of intermediates. In general, there are several approaches to stimulate CO_2 activation:

(1) Defect engineering, such as introducing non-stoichiometric tungsten oxide (WO_{3-x}), which is rich in surface oxygen vacancies (V_O), can lead to the generation of LSPR in the visible and infrared regions. This unique characteristic enhances WO_3's light-harvesting ability, resulting in improved carrier separation [13]. Defects also provide additional adsorption sites for CO_2 activation, thereby reducing reaction barriers and modifying the product distribution [27].

(2) Modulating surface basic sites offers an alternative approach for CO_2 adsorption and activation [28]. Alkaline modification of W_xO_y-based catalysts' surface enhances CO_2 adsorption performance. The reaction between the acidic CO_2 and the alkaline surface of the photocatalyst results in the formation of intermediates, such as bicarbonate, favoring the activation and subsequent reduction of CO_2 molecules.

(3) The decoration of metal co-catalysts has been demonstrated to promote CO_2 activation [29]. When a W_xO_y-based catalyst is excited, the generated electron-hole pairs separate, with the electrons and protons transferred to the catalyst or co-catalyst surface. The electrons are involved in the reduction of CO_2 at the active sites of the W_xO_y-based catalyst or co-catalyst, while the protons participate in the oxidation reaction of water.

2.2. General reaction pathways for CO_2-PR

2.2.1. C1 production

CO_2-PR involves a series of fundamental steps, including electron/proton (e^-/H^+) transfer, C=O bond cleavage, intermediate formation, and new bond formation [30].

The photo-generated electrons in the conduction band (CB) can engage in CO_2-PR to produce renewable hydrocarbon fuels (equation: $CO_2 + H_2O \rightarrow \text{hydrocarbons} + O_2$) under mild reaction conditions, typically at room temperature and pressure. Conversely, the holes in the valence band (VB) generally take part in the oxidation of water [31]. Furthermore, CO_2-PR exhibits a wide range of potential catalytic products, including CO, HCOOH, CH_2O, CH_3OH, CH_4, C_2H_5OH, and others. The reaction can involve a catalytic process requiring 2–12 electrons (Eqs. 1–8). In the following equations, E^0 represents the potential of the electrode under standard hydrogen electrode reference conditions.

$$CO_2 + 2H^+ + 2e^- \rightarrow HCOOH,\ E^0 = -0.61\ \text{V} \tag{1}$$

$$CO_2 + 2H^+ + 2e^- \rightarrow CO + H_2O,\ E^0 = -0.53\ \text{V} \tag{2}$$

$$CO_2 + 4H^+ + 4e^- \rightarrow HCHO + H_2O,\ E^0 = -0.48\ \text{V} \tag{3}$$

$$CO_2 + 6H^+ + 6e^- \rightarrow CH_3OH + H_2O,\ E^0 = -0.38\ \text{V} \tag{4}$$

$$CO_2 + 8H^+ + 8e^- \rightarrow CH_4 + 2H_2O,\ E^0 = -0.24\ \text{V} \tag{5}$$

$$2CO_2 + 12H^+ + 12e^- \rightarrow C_2H_5OH + 3H_2O,\ E^0 = -0.33\ \text{V} \tag{6}$$

$$2H^+ + 2e^- \rightarrow H_2,\ E^0 = -0.41\ \text{V} \tag{7}$$

$$2H_2O + 4h^+ \rightarrow O_2 + 4H^+,\ E^0 = +0.82\ \text{V} \tag{8}$$

Habisreutinger *et al.* [32] summarized three potential mechanisms for CO_2-PR to generate C1 products (CO, HCOOH, CH_2O, CH_3OH, and CH_4), as well as some C2 products, including formaldehyde pathway, carbene pathway, and glyoxal pathway. The differentiation among these pathways arises from the various modes of CO_2 adsorption on the surface of the catalysts, encompassing oxygen coordination, carbon coordination, and lateral/mixed coordination. Regardless of the pathway, the reaction commences with the adsorption and activation of CO_2, leading to the formation of charged $CO_2^{\bullet-}$ species on the catalyst's surface. The discrepancies in these pathways stem from the distinct manners in which $CO_2^{\bullet-}$ binds to the catalysts. The final product of all three pathways is CH_4, and CH_3OH is produced in both the formaldehyde pathway and the carbene pathway.

However, Koci *et al.* [33] found that the distribution of CH_4 and CH_3OH did not align with the formaldehyde pathway alone, as CH_3OH is not an intermediate in the production of CH_4. To address this, Wang *et al.* [34] proposed a new formyl pathway (Fig. S2 in Supporting information) that integrates the formaldehyde, carbene, and glyoxal pathways. In the formyl pathway, if the catalyst possesses moderate adsorption strength, the C-anchored CO intermediate can accept an e^-, while a H^+ attacks the C atom to form CHO. With the assistance of another e^-/H^+, CHO can be further converted into CH_2O. Subsequently, the intermediate becomes successively bonded to C by binding with the e^-/H^+ until it eventually produces CH_3OH or CH_4.

2.2.2. C2 production

C2 production have garnered significant attention due to their higher economic benefits, making the direct generation of C2 production through CO_2-PR a current hot research topic. The synthesis of the C2 product poses a greater challenge compared to the synthesis of the C1 product due to the requirement of a higher concentration of electrons in the active site [35]. The key to further generating C2 products lies in the dimerization of C1 intermediates on the catalyst surface to form C–C bonds. Furthermore, it is crucial for the intermediates to strongly bond to the catalyst surface to generate C2 products instead of early desorption as C1 products, such as CO and CH_2O. Fig. S3 (in Supporting information) depicts three pathways for generating C2 and C_{2+} products.

2.3. Working parameters

The CO_2-PR process is influenced by various parameters, including temperature, medium pH, CO_2 partial pressure, light intensity and wavelength, H_2O partial pressure and reaction system. These parameters play a significant role in determining the CO_2-PR conversion and product selectivity. Consequently, this subsection provides a comprehensive analysis of the influence mechanisms associated with different reaction conditions.

2.3.1. Temperature

The initiation of a photocatalytic reaction necessitates a driving force that generates the electron-hole (e^--h^+) pair. This driving force is provided by light irradiation in the form of the Gibbs free energy (ΔG). Previous studies have observed that the rate of CO_2-PR increases at higher temperatures due to the augmentation in collision frequency and diffusion rate of the reactant molecules [36]. This implies that higher temperatures are more conducive to enhancing the mass transfer rate of CO_2 from the surface of the photocatalyst, consequently improving the overall reaction rate. Additionally, higher temperatures expedite the reaction rate by reducing the activation energy needed to initiate chemical reactions.

2.3.2. pH value

The solvent's pH is a crucial factor in enhancing the rate and efficiency of CO_2-PR. Variations in protons concentration within the reaction medium influence the theoretical reduction potential of CO_2 when it functions as both a reactant and a buffer. Additionally, high pH favors the decomposition of CO_2 into $CO_3{}^{2-}$ or $HCO_3{}^-$, which possess varied standard redox potential values, affecting their adsorption properties on the photocatalyst surface and consequently leading to different product yields and selectivity. For instance, Das *et al.* [37] discovered that higher pH levels are correlated with increased CO_2 solubility, elevated CO_2 concentration near the catalyst's surface, and improved CO_2 reduction efficiency. However, excessively high pH levels restrict the supply of surface adsorbed H^+ to the adsorbed $^*CO_2$, thereby hindering further CO_2-PR.

2.3.3. CO_2 partial pressure

The photoconversion rate of CO_2 is heavily influenced by the adsorption rate of CO_2 molecules on the photocatalyst's surface. This adsorption process relies on the van der Waals force governing the interaction between the adsorbent (photocatalyst) and the adsorbate (CO_2). This force acts as an adhesion force within the adsorbate-adsorbent system and strengthens with increasing partial pressure of the adsorbate. Consequently, higher partial pressure of CO_2 gas leads to better product yields when CO_2 is in the gas phase. In both gas-phase and liquid-phase systems, the partial pressure of CO_2 (P_{CO_2}) regulates the likelihood of adsorption on the photocatalyst's active sites, thereby ensuring higher yields of solar fuels.

2.3.4. Light intensity and wavelength

Regarding energy considerations, light intensity and wavelength play pivotal roles in photocatalytic reactions. The energy possessed by the excited e^--h^+ pairs relies on the wavelength of light, while the number of e^--h^+ pairs is contingent upon the intensity of light. Research conducted by Ikreedeegh *et al.* [38] observed that the CO_2-PR demonstrated heightened activity with increasing light intensity, yet decreased activity when exposed to longer light wavelengths. Higher-power lamps emit a greater quantity of photons and generate a larger number of e^--h^+ pairs. However, even with high-power lamps, photogenerated e^- and h^+ can still undergo rapid recombination, thereby diminishing photocatalytic efficiency [39].

2.3.5. HER

The process of H_2O splitting plays a crucial role in CO_2-PR, where H_2O molecules interact directly with excited state e^- in the CB and h^+ in the VB to generate H_2 and O_2 [40]. The recombination of the e^--h^+ pairs can be prevented by h^+ consuming OH^- species [41]. A minimum band gap of 1.23 eV is required for the photocatalytic decomposition of water. In the case of W_xO_y-based catalysts, the bandwidth ranges from 2.5 to 2.8 eV. As a result, the hydrogen evolution reaction (HER) can compete with CO_2-PR due to its higher kinetic feasibility. Furthermore, the slow diffusion of CO_2 molecules on the catalyst surface and the involvement of H_2O in generating H_2 during the reaction can decrease the availability of H^+ for CO_2 reduction, thereby reducing both the activity and product selectivity of CO_2-PR. Consequently, photocatalysts must exhibit elevated activity for H_2O oxidation while limiting excessive H_2 generation.

2.3.6. Reaction system

CO_2-PR is conducted in gas-liquid-solid or gas-solid systems. In gas-liquid-solid systems, co-solvents are added to increase the solubility of CO_2, as well as sacrificial agents to inhibit competing half-reactions, making it easier to detect liquid-phase products, including formic acid. For gas-solid systems, the yield of gaseous products such as CH_4 is relatively high. For smooth CO_2 hydrogenation, a balance of water vapor and CO_2 molecule adsorption on the surface of the material is required, as well as the ability to inhibit the HER [42]. Additionally, without extra sacrificial agents, the surface of the catalyst is exposed to the accumulation of $\cdot OH$ after the depletion of H^+, leading to the deactivation of the catalyst. Recently, three-phase photocatalysis has emerged as a promising solution to address mass transfer limitations in CO_2-PR. The efficiency of three-phase photocatalysis lies in its ability to rapidly transport CO_2 to the catalyst surface [43]. Moreover, e^--h^+ pairs play a pivotal role in regulating CO_2-PR, and their effective separation is achieved through external or internal electric fields [44]. Despite these advantages, challenges persist in the photoreduction of insoluble stable gas molecules, including hindered kinetic diffusion, sluggish surface adsorption, and inefficient activation of gaseous reactants at three-phase catalytic interfaces [45].

To achieve higher yields and superior product selectivity in CO_2-PR, careful selection of all the parameters is necessary. Moreover, there is a need for not only efficient and robust photocatalysts, but also sustainable interfacial photocatalytic systems.

3. W_xO_y-based materials

Although W_xO_y-based materials possess appropriate band gaps, they exhibit limited catalytic reactivity, including low sunlight utilization, low surface negative charge density, fast recombination of photogenerated e^--h^+ pairs, and low carrier migration efficiency. Various approaches have been explored to enhance the efficiency of photocatalytic systems, such as morphology engineering, elemental doping, and heterojunction formation [46-48]. The W_xO_y-based photocatalysts for CO_2-PR are showed in Table S1 (Supporting Information). These modifications will be discussed in greater detail below.

3.1. *Defects/phase/facet*

For metal-oxide semiconductors, an alternative and cost-effective method to increase the surface negative charge density and improve CO_2-PR performance is by constructing surface V_O. The presence of V_O serves two important functions: (I) It promotes the activation of reactants, leading to the formation of active substances; (II) It expands light absorption, thereby enhancing the efficient utilization of solar energy [49]. While CO_2-PR driven by WO_3 is mainly dominated by C1 products (such as CO and CH_4), WO_{3-x} can enhance the efficiency of C–C coupling and reduce CO_2 to C2 products.

Although V_O exhibits better ability in increasing the negative charge density on the surface, it is easily inactivated through oxidation due to its typically low concentration on the surface. However, Sun *et al.* [50] successfully synthesized ultrathin $WO_3{\cdot}0.33H_2O$ nanotubes with a high level of exposed surface V_O. During the generation of CH_3COOH, the V_O that adsorbed CO_2 could be easily separated from V_O after forming C–C bonds, enabling sustainable utilization of V_O and suppressing V_O inactivation. Moreover, Deng *et al.* [51] prepared ultrathin WO_{3-x} nanosheets with oxygen defects. Theoretical calculations confirmed that these defects are crucial in the reduction of CO_2 to C2 hydrocarbons, and V_O promoted the C–C coupling of the reduced C–H intermediates, effectively preventing the complexation of photogenerated e^- and h^+, thereby improving the conversion efficiency of WO_{3-x} to CO_2.

The presence of photo-induced V_O is a double-edged sword. While a small amount of V_O enhances the photocatalytic activity, an excessive amount of V_O can disrupt the hexagonal WO_3 structure, leading to a decrease in photocatalytic activity. Wang *et al.* [52] successfully synthesized V_O-containing samples by treating hexagonal WO_3 in an atmosphere containing H_2 and demonstrated that this V_O generation process is reversible when the catalyst is exposed to an atmosphere containing O_2. The photocatalytic activity significantly increases with the increase in V_O content, reaching its maximum value.

Stoichiometric WO_3 is comprised of edge-shared octahedral WO_6. It exhibits heterogeneous phases, including monoclinic, tridiagonal, orthorhombic, tetragonal, hexagonal, and cubic phases. The specific phase depends on the angle of lattice tilt and the direction of rotation [53]. In room temperature, monoclinic I has the most stable structure, which is a typical n-type semiconductor with a band gap of 2.62 eV. $W_{18}O_{49}$ has a unique monoclinic structure and has been widely studied for its ability to exhibit a strong LSPR effect and excellent CO_2-PR performance. Monoclinic and hexagonal crystals are the most promising options among the various crystalline phases. The monoclinic phase is known for its stability, while the hexagonal phase possesses an open-hole structure and abundant intercalation chemistry [54]. Both WO_{3-x}/$GdCrO_3$ and WO_{3-x}-R/$GdCrO_3$ consist of monoclinic crystals $W_{18}O_{49}$ and orthorhombic crystals $GdCrO_3$. The close contact between WO_{3-x}-R and $GdCrO_3$ is clearly observed in the HRTEM image (Fig. 1a). The growth of WO_{3-x} nanosheets with plentiful defect sites on $GdCrO_3$ along the [−1,0,4] direction is evident. Simultaneously, the crystal surface of WO_{3-x} can be meticulously crafted to expose a greater number of active sites [55]. At the WO_{3-x}-R/$GdCrO_3$ interface, $W^{5/4+}$ defect sites are introduced, serving as a bridge for photothermal-induced charge storage, secondary plasmon excitation, and interband transfer, as seen in Fig. 1b. This approach enables efficient charge separation, high redox potential, and sufficient absorption of visible light [56].

Non-stoichiometric tungsten oxide (WO_{3-x}) possesses a high density of V_O and shows LSPR in the visible-near-infrared region. The presence of V_O in WO_{3-x} results in broad absorption in both the visible and infrared regions. Li *et al.* [57] observed a gradual transition from WO_3 to $W_{18}O_{49}$ during carbothermal reduction at temperatures higher than 800 °C. The introduction of W^{5+} on the

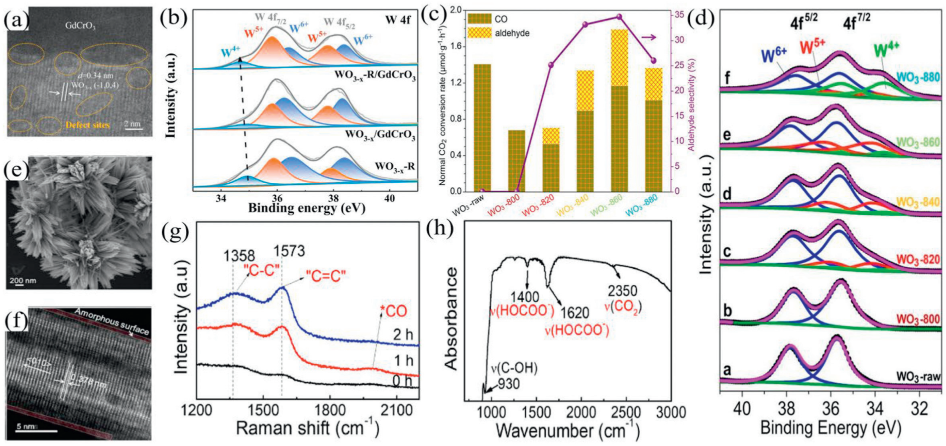

Fig. 1. (a) HETEM of WO_{3-x}-R/$GdCrO_3$, and (b) W 4f XPS spectra of the samples. Reprinted with permission [56]. Copyright 2022, Elsevier. (c) CO_2 photoelectrocatalytic performances of WO_3-raw and WO_3-T, and (d) XPS W 4f profiles of WO_3-raw and WO_3-T. Reprinted with permission [57]. Copyright 2020, Elsevier. The aldehyde selectivity of the catalysts is represented by dots, SEM (e) and HAADF-STEM (f) images of WO_{3-x}-2 synthesized under 2 mL HCl assistance, Raman spectra (g) of WO_{3-x}-2 during CO_2-PR, and their IR spectra (h) after photocatalysis. Reprinted with permission [58]. Copyright 2020, Elsevier.

surface of non-stoichiometric WO_3 facilitated the selective conversion of CO_2 to aldehyde with a 35% yield (Fig. 1c). This phase transition led to the presence of low-valent surface components, such as W^{5+} and W^{4+}, alongside the initial W^{6+} material in different ratios (Fig. 1d), which assembled the surface structure of non-stoichiometric WO_3-T. Lu *et al.* [58] performed plasma synthesis of WO_3 with tunable Vo and low-valence W ions. They observed a sea urchin-like structure of WO_{3-x}-2 (Fig. 1e), with a clear and ordered lattice structure corresponding to the (010) face observed by atomic resolution high-angle annular dark-field scanning transmission electron microscopy (HAADF-STEM) (Fig. 1f). Raman and IR (Figs. 1g and h) spectroscopy revealed the presence of "C=C", "C–C", adsorbed CO, HOCOO, and adsorbed CO_2 intermediates on the WO_{3-x}-2 surface, indicating that adjacent V_O provide active sites for C–C coupling to ethylene.

Surface modification of W_xO_y-based photocatalysts using the characteristics of WO_3, such as the introduction of abundant defect sites and the dominant monoclinic phase structure, can significantly enhance the CO_2 adsorption capacity and provide reactive active sites for the selective production of C1 and C2 products.

3.2. Doping

Exogenous ion doping is a simple and effective method to modulate the electronic structure of photocatalysts, altering the valence state of the element and facilitating the introduction of low-valence metal species into WO_3 [59,60]. Furthermore, elemental doping can induce the formation of intermediate energy bands or V_O, optimizing the band structure of the photocatalysts [61]. Importantly, since the CO_2-PR occurs on the catalyst surface, the surface doping of metal ions on the photocatalyst can promote CO_2 adsorption capacity and the transfer of photogenerated carriers [62].

For instance, Wang *et al.* [63] synthesized Mo-doped $WO_3 \cdot 0.33H_2O$ nanorods. As illustrated in Fig. 2a, the electron paramagnetic resonance (EPR) spectra demonstrated a significant increase in the V_O content of Mo-doped $WO_3 \cdot 0.33H_2O$, which facilitated the supply and insertion process of H^+ and improved the hydrogenation process of carbon intermediates for CH_4 generation. This ultimately resulted in an increase in CH_4 yield, as shown in Fig. 2b. And Fig. 2c shows the scheme of Mo-doped $WO_3 \cdot 0.33H_2O$ CO_2 reduction reaction with H_2O driven by solar energy. Zhang *et al.* [64] doped Cu^+ into the $W_{18}O_{49}$ nanowires. Analysis of the fitted peaks of W 4f revealed an increase in the content of W^{5+} after Cu^+ doping. In addition, the peaks of W 4f shifted towards high binding energies, as depicted in Fig. 2d. The EPR spectrum (Fig. 2e) confirmed the increase in V_O content due to Cu^+ doping, with the EPR signal of Cu-$W_{18}O_{49}$–0.005 being significantly higher than that of pure $W_{18}O_{49}$. Cu^+ served as an active site for CO_2 activation, shifting its conduction band to a more negative position and served as an electron transfer center, reducing e^--h^+ pair recombination and enhancing charge transfer.

Yi *et al.* [65] discovered that the co-doping of Mo and Cs in reduced WO_3 improved CO_2-PR performance compared to solely modified WO_3. The band gap of CsWO was slightly narrowed by Mo doping, increasing the light absorption capacity of CsWO and inducing a reductive Mo^{5+} for the LSPR effect. Therefore, narrowing the band gap of W_xO_y-based materials is also an important strategy for enhancing CO_2-PR performance.

Doping metal elements into W_xO_y-based photocatalysts serves to modulate the edge positions of VB and CB, while also inhibiting carrier recombination and promoting the formation of V_O. This synergistic interaction with neighboring ligand-unsaturated metal ions, hydroxyl groups, and ions enhances the photocatalytic performance.

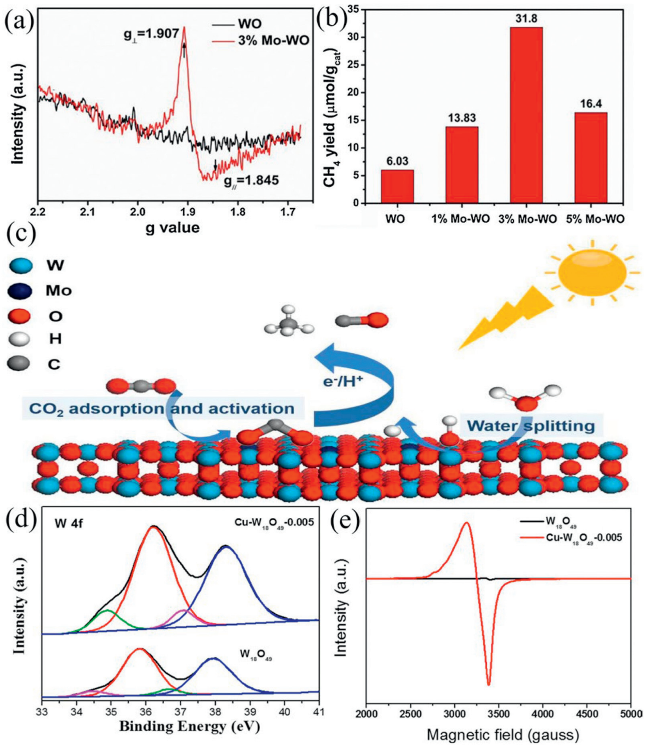

Fig. 2. (a) EPR spectra at 300 K for WO and 3% Mo-WO, (b) The yield of CO_2-PR to CH_4 in the first 6 h for WO, 1% Mo-WO, 3%Mo-WO and 5%Mo-WO, and (c) CO_2-PR over Mo-WO with water under solar irradiation. Reprinted with permission [63]. Copyright 2019, Elsevier. (d) W 4f high-resolution XPS spectra and (e) room-temperature EPR spectra of $W_{18}O_{49}$ and Cu-$W_{18}O_{49}$–0.005. Reprinted with permission [64]. Copyright 2020, Elsevier.

3.3. Composite materials

Single-component photocatalysts face a challenge in providing both strong redox capacity and a broad-range photoresponse. This is because achieving the former requires a large bandgap, while the latter necessitates a narrow bandgap [66]. Moreover, in single-component nanophotocatalysts, the generated e^--h^+ pairs are often prone to recombination due to strong coulombic interactions. It will result in a significant loss of photogenerated charge [67]. The construction of semiconductor heterojunctions has proven to be an effective strategy. Heterojunctions enable a wide range of photoresponse and promote efficient charge separation, thereby enhancing the strong redox capacity that facilitates CO_2-PR [68].

3.3.1. Binary composites

Among the semiconductors with high VB potentials, WO_3 has attracted significant attention from researchers due to its high specific surface area, high visible light activity, and high oxidation potential. However, WO_3 has positive CB position, which is ineffective for CO_2 reduction. Additionally, its narrow band gap leads to rapid recombination of charge carriers, resulting in poor photocatalytic activity. To address these limitations, WO_3 can be combined with semiconductors that have negative VB positions to form composite heterojunctions, thus facilitating efficient separation of e^--h^+ pairs and enhancing the performance of CO_2-PR.

WO_3 is commonly used as the oxidation component in Z-scheme heterojunction composites due to its positive VB potential and ability to oxidize photogenerated holes. For example, Tahir *et al.* [69] created Z-scheme WO_3/g-C_3N_4 heterojunction that allowed efficient interaction between the two semiconductors and achieved effective carrier separation. Jiang *et al.* [70] found that good performance of the $CsPbBr_3/WO_3$ heterojunction was attributed to the Z-scheme mechanism with a strong internal electric field. Tang *et al.* [71] designed a three-dimensionally ordered macroporous (3DOM) structure of WO_3 with a slow photon effect. Additionally, they grew g-C_3N_4 thin films on the surface of 3DOM-WO_3 *in situ*. This approach effectively addresses the limitation caused by the mismatch between the conduction band position of conventional semiconducting materials and the required redox potential for the reaction. Consequently, directional conduction of electrons between the two semiconductor materials is achieved, enhancing the efficiency of visible light trapping. These studies demonstrate the potential of using WO_3 as an efficient visible light-active co-catalyst for constructing heterojunctions for CO_2-PR.

Yu *et al.* [72,73] proposed novel S-scheme heterojunction photocatalysts that using a distinct electron transfer mechanism compared to conventional type II and Z-scheme heterojunctions. Comparatively, S-scheme heterojunctions consisting of a reduced semiconductor and an oxidized semiconductor exhibit improved charge separation and enhance the kinetic of CO_2-PR. Additionally, they fulfill the thermodynamic requirements for CO_2-PR [74,75]. For instance, the ultrasound-assisted $Cs_2AgBiBr_6/Bi_2WO_6$ nanocomposites, featuring a staggered-band arrangement of S-scheme heterojunction structures, and the one-dimensional S-scheme heterojunction structure of SiC-$W_{18}O_{49}$, characterized by a distinctive sea urchin morphology, both demonstrate enhanced CO_2-PR performance compared to individual materials [76,77].

Recently, the use of 2D/2D interfaces has demonstrated effectiveness in providing larger contact interfaces, reducing carrier transport distances, and increasing the availability of active sites [78,79]. Jiang *et al.* [80] exploited the synergistic 2D/2D interface (Fig. 3a), Vo-induced defect energy levels (Figs. 3b and c), achieved a significant CO evolution rate increase in the 30V_O-WO_x/BiOCl, which is 4.68 and 3.09 times higher than that of BiOCl and 30WO_3/BiOCl, respectively (Figs. 3d and e). And S-scheme transfer modes of V_O-WO_x/BiOCl composites (Fig. 3f) to achieve faster V_O-WO_x and BiOCl dual transfer modes through carrier separation and improved charge separation and transfer efficiency.

In addition, a distinctive feature of WO_3 is its ability to have carefully designed V_O states that exhibit broad and strong absorption in the near-infrared (NIR) region [81]. Huang *et al.* [82] constructed plasma-enhanced S-scheme WO/CdSe-D photocatalysts. The abundant V_O in WO_3 induced LSPR effect, extending the light absorption range of WO/CdSe-D to the NIR region, thus enhancing absorption in the visible and NIR regions. Therefore, the rational utilization of WO_3's properties offer the potential to develop composite photocatalysts for NIR CO_2-PR.

Binary semiconductor composites offer several advantages, including improved optical response range, enhanced separation and transport of photogenerated carriers, and increased reactive interfaces and active sites. CB position of W_xO_y enables the effective electron transport and separation of photogenerated carriers when combined with semiconductor materials such as TiO_2 and $BiVO_4$, which have a negative VB position. As a result, these composites can significantly enhance CO_2-PR activity.

3.3.2. Ternary composites

In addition to binary composites, more complex structures, such as ternary catalysts, have also been reported, which can be derived from one or a combination of the structures. Ternary composites have garnered significant attention from researchers due to their ability to facilitate the rapid migration of excited electrons [83].

Studies have demonstrated that ternary components exhibit superior photocatalytic activity compared to binary components. Jiang *et al.* [84] proposed the concept of plasma-active "hotspot" confined photocatalysis, where the coexcited LSPR of Au and $W_{18}O_{49}$ components form metal/non-metal coupled plasma coupling hotspots within a sandwich-like substructure of the Au/TiO_2/$W_{18}O_{49}$ plasma heterostructure (Figs. 3g and h). In comparison to a single-plasma-component system

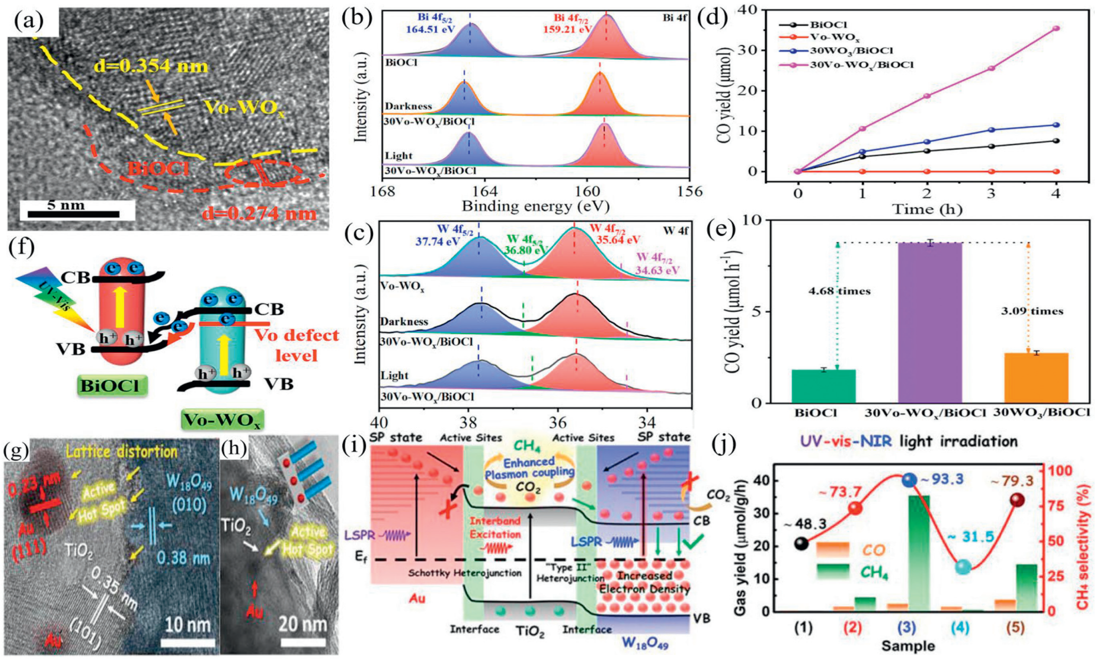

Fig. 3. (a) HRTEM of the 30V_O-WO_x/BiOCl sample, high-resolution XPS spectra of Bi 4f (b), W 4f (c) of the BiOCl, V_O-WO_x and 30V_O-WO_x/BiOCl samples in the dark and under the light, (d) the CO evaluation of BiOCl, V_O-WO_x. 30WO_3/BiOCl and 30V_O-WO_x /BiOCl, (e) CO production rates of BiOCl, 30WO_3/BiOCl and 30V_O-WO_x/BiOCl, and (f) S-scheme heterojunction composed by BiOCl and V_O-WO_x. Reprinted with permission [80]. Copyright 2022, Elsevier. (g) HRTEM image of the Au/TiO_2/$W_{18}O_{49}$ plasmonic heterostructure, (h) TEM image of the side view of the Au/TiO_2/$W_{18}O_{49}$ plasmonic heterostructure, (i) schematic diagram showing the hot electron generation and transfer processes due to the enhanced plasmon coupling between Au and $W_{18}O_{49}$ under UV–vis–NIR light irradiation, and (j) gas productions and the corresponding CH_4 selectivity through CO_2-PR over the as-synthesized samples under UV–vis–NIR light irradiation: (1) TiO_2 NFs, (2) Au/TiO_2 composite NFs, (3) Au/TiO_2/$W_{18}O_{49}$ plasmonic heterostructure, (4) $W_{18}O_{49}$ NWs, (5) $W_{18}O_{49}$/TiO_2 plasmonic heterostructure. Reprinted with permission [84]. Copyright 2022, Wiley-VCH.

(Au/TiO_2 or $W_{18}O_{49}/TiO_2$), the two-plasma-component system ($Au/TiO_2/W_{18}O_{49}$) can generate more thermally excited electrons for CO_2-PR (Fig. 3i) when the LSPR of Au and $W_{18}O_{49}$ components and the interband leaps of the TiO_2 component are co-excited. This configuration leads to efficient CO_2-PR (Fig. 3j). In the ternary system constructed by Dong *et al.* [85], the $WO_3/CsPbBr_3$ Z-scheme heterojunction provided an effective pathway for the transfer of photogenerated charge carriers. This ternary system was further modified with ZIF-67 to enhance charge separation and improve CO_2 adsorption performance. The evaluation of CO_2-PR activities revealed that after 3 h of irradiation, the CO yield of $WO_3/CsPbBr_3$ was 3.6 times higher than that of bare $CsPbBr_3$. Further modification with ZIF-67 resulted in the highest CO yield of 99.38 µmol/g, which was 6.8 times higher than that of $CsPbBr_3$. The porous structure also contributed to a higher specific surface area, increased adsorption sites, and multiple transfer pathways during the photoreduction process. These results highlight the significant contribution of ternary components to the enhancement of CO_2-PR performance.

While multicomponent catalysts demonstrate clear advantages in improving CO_2-PR activity compared to single-component catalysts, the complexity of their preparation procedures raises the need for further investigation regarding whether the composite between various materials can achieve the theoretical effects. Considering factors such as cost and photocatalytic efficiency, current research on binary composites remains more extensive. However, there are still numerous possibilities awaiting exploration in the realm of ternary composites.

4. Performance evaluation of W_xO_y-based catalysts

4.1. Yield

The metal atoms were incorporated into the W_xO_y-based catalysts through surface modification engineering to enhance the separation and transfer efficiency of CO_2-PR charges. Pd underwent the H_2 spillover effect to form hydrotungsten bronze, which facilitated H_2 dissociation and spillover. WO_3, on the other hand, stored H^+ and e^- as hydrotungsten bronze within its lattice [86]. Furthermore, the Co-modified $W_{18}O_{49}$ demonstrated efficient carrier separation with positive facilitation. The isolated Co atoms acted as an electron pump, promoting charge separation and transport efficiency, and accelerating CO_2-PR kinetics [87]. Both modifications resulted in increased photocatalytic efficiency for bulk CO production, yielding 7.5 and 21.18 $mmol\,g^{-1}\,h^{-1}$, respectively. Moreover, the study revealed that loading Pd and Au bimetals into TiO_2-WO_3 as CO_2-PR active sites effectively suppressed the complexation of photoexcited e^--h^+ pairs [88].

The activity of CO_2-PR is influenced by various factors, including temperature, light intensity, reaction time, catalyst loading, H_2O/CO_2 molar feed ratio, among others. Yi *et al.* [65] observed that the co-doping of Mo and Cs with WO_3 effectively improved CO_2-PR efficiency. However, the samples exhibited the highest activity in producing CO and CH_3OH when the doping concentration of Mo was 5%, and the activity decreased with an increase in the doping concentration to 10%. This decrease may be due to excessive Mo doping, which can cause certain Mo sites to become capture centers, hindering charge separation. WO_3-TiO_2/Cu_2ZnSnS_4 composites deactivated during CO_2-PR due to the formation of residual organics. After continuous irradiation for 5 h, the yields of both reduction products slightly decreased [89]. Furthermore, reaction conditions, such as the concentration of protons from water vapor, can easily affect the yield of CH_4, which resulting in a more pronounced decrease in CH_4 yield compared to CO yield.

Currently, many photocatalysts primarily produce C1 products. There are several photocatalysts that have shown high yields of CO and CH_4. For example, melamine foam-loaded 1.5 mg $WO_3/CsPbBr_3$ composites, placed in a 100 mL polytetrafluoroethylene reactor with the addition of 4 mL DI water, reacted under 300 W Xe lamp irradiation for 2 h. This resulted in a high CO yield of 351.83 $mmol\,g^{-1}\,h^{-1}$ (Fig. S4a in Supporting information) [90]. In other experiments, Tahir *et al.* [69] found that a WO_3/g-C_3N_4 photocatalyst, loaded with 25 wt% WO_3 at a quantity of 150 mg, achieved a CH_4 yield of 226 $mmol\,g^{-1}\,h^{-1}$. The reaction conditions included a temperature of 40 °C, 20 W Xe HID lamp source irradiation, and a gas-solid H_2O/CO_2 feed ratio of 0.4 (Figs. S4b and c in Supporting information).

In summary, to realize the optimal activity of tungsten-based catalysts on CO_2-PR, firstly, suitable mono/bimetallic co-catalysts should be found, such as Pd and Co, which can store H^+ and e^-. Searching for semiconductor materials that can narrow the band gap of W_xO_y to form heterojunctions for efficient photogenerated e^- separation and transport. Meanwhile, the parameters can be tuned in the reaction system to optimize the photocatalytic activity, and the optimal reaction conditions can be achieved by controlling the metal loading, temperature, pressure, saturated vapor pressure, and light intensity. The activity of photocatalysts in promoting CO_2-PR is influenced by several factors, hence the need for multiple optimizations to enhance CO_2-PR efficiency.

4.2. Selectivity

The efficiency of photocarrier separation, photoexcitation, and the energy-band structure influence the CO_2-PR activity and product selectivity of different tungsten-based materials [91]. Selectivity is usually calculated in two ways, one is the carbon balance (Eq. 9) and the other is the electron balance (Eq. 10). Assessing product selectivity is crucial in evaluating CO_2-PR activity.

$$\text{selectivity}: \ \frac{n_{\text{target products}}}{n_{\text{total products}}} \tag{9}$$

$$\text{selectivity}: \ \frac{N_e(x) \times n(x)}{\sum_i \left[N_e(i) \times n(i)\right]} \times 100\% \tag{10}$$

During the multistep surface-catalyzed reaction of CO_2 reduction, the adsorption and desorption characteristics of the reactants and intermediates are key kinetic factors influencing product selectivity. Feng *et al.* [92] proposed a novel “atomic-level single-site” strategy to achieve a CH_4 selectivity of 86.5%, exceeding that of pristine TiO_2 by an order of magnitude. Jiang *et al.* [84] found that unique bis-heteroactive sites (Au-O-Ti and W-O-Ti) embedded on the plasma-coupled hotspots of the $Au/TiO_2/W_{18}O_{49}$ plasma heterostructures could adsorb the produced CO and H^+ and facilitate further reduction of CO to CH_4 through plasma-induced high-energy thermoelectronics.

Meanwhile, the abundance of active sites on the surface of WO_3 enables the introduction of V_O, which contributes to its unique structural features that promote C–C coupling and selective generation of more C2 products during the CO_2-PR process. Lu *et al.* [58] demonstrated that $WO_{3\text{-}x}$-2, with the highest V_O content, exhibited optimal ethylene-generating activity and selectivity in CO_2-PR under full-spectrum light irradiation (89.3% selectivity). This selectivity was 20 times higher than that of $WO_{3\text{-}x}$-0, which had low V_O content and a thick amorphous surface (17.5% selectivity). The combined effect of UV, visible, and NIR radiation synergistically enhanced the activity and selectivity of plasma $WO_{3\text{-}x}$-2 in acetylene production (Figs. S4d and e in Supporting information). Shen *et al.* [93] prepared $TiO_{2\text{-}x}$ and $WO_{3\text{-}y}$, which formed an effective Z-scheme heterojunction with V_O as the interfacial layer. The synergistic effect of defects and the heterojunction promoted the separation and transport of photogenerated carriers. Furthermore, when loaded with Pd as a co-catalyst, the selectivity of CH_4 was increased to 100%. The presence of the co-catalyst significantly enhanced the selectivity of CO_2-PR products (Fig. S4f in Supporting information).

The selectivity of reduction products is strongly influenced by the CO_2-PR pathway, particularly in the case of multicarbon products. Structural modulation enables the utilization of abundant defect sites, which in turn induce C–C coupling. This modulation has several effects, such as accelerating the adsorption of CO_2 on the photocatalyst surface, enhancing the desorption of intermediates, introducing metal atoms to increase reactive sites, facilitating the transfer of photogenerated electrons and holes involved in CO_2-PR, constructing special heterojunction structures to improve carrier separation efficiency, and reducing the free energy barriers for the conversion of CO_2 into CH_4, CH_3COOH, and other products. These modifications allow for the selective generation of a greater variety of desired target products in CO_2-PR.

4.3. Stability

High interfacial catalytic activity is often accompanied by side reactions, such as photonic corrosion [94] and structural remodeling [95], which can lead to the deactivation of pre-designed catalysts. In the case of CO_2-PR, the selectivity of products and the adsorption of specific intermediates are highly correlated. However, strong adsorption can block the active site and alter the electronic structure of the catalytic surface, ultimately poisoning and deactivating the catalyst [96]. The stability of photocatalysts is crucial for their practical application and determines their ability to be reused without significant loss of activity [97]. Therefore, a fundamental principle in catalyst design is to balance the activity and stability of the catalysts.

To assess the reusability of photocatalysts, researchers conducted multiple or cyclic degradation tests using the same composite. Yi *et al.* [65] demonstrated that the 5% Mo-CsWO samples maintained good photocatalytic stability after four testing cycles. XRD and XPS analysis revealed that the structures, surface properties, and compositions of the catalysts remained largely unchanged compared to the pristine sample, indicating excellent structural stability of Mo-CsWO. Similarly, $W_{18}O_{49}$@Co exhibited high durability in cycling tests, consistently demonstrating significant photocatalytic activity throughout each cycle. Characterization of the catalyzed $W_{18}O_{49}$@Co showed no noticeable changes in structure or loss of CO content during the reaction [87]. Jiang *et al.* [70] prepared a $CsPbBr_3/WO_3$ heterojunction, which showed only a slight 2.6% decrease in activity after four catalytic runs (2 h per cycle), while maintaining the same morphology and phase as the catalysts. This improved stability of CPB NCs in heterojunctions could be attributed to their Z-scheme charge transfer mode, where the photogenerated h^+ of CPB was consumed by the photogenerated e^- of WO_3, preventing the accumulation of photogenerated h^+ on the CPB side, which is susceptible to photocorrosion (Figs. S4g and h in Supporting information) [98].

However, certain W_xO_y-based photocatalysts have shown limitations in terms of cycling stability during CO_2-PR. In a study by Zeng *et al.* [99], the 3% Cu/WO_3 catalyst maintained a stable crystalline structure after cycling experiments. However, a degradation in catalyst performance was observed during the cycling test. Residual products on the used 3% Cu/WO_3 catalyst weakened the adsorption strength of CH_3COOH for CO_2, and the reduction of Cu^+ sites led to a decrease in its C–C coupling ability, ultimately reducing CO_2-PR activity. Moreover, Shi *et al.* [100] found that the CO_2-PR process induced an excess increase of W^{5+} in Cu_2O/WO_3–001 composites, which would lead to poorer performance of CO_2-PR even after electrochemical regeneration.

Many W_xO_y-based materials possess remarkable stability in their structures, surface properties, and compositions, which is crucial to prevent degradation of the photocatalyst performance. Firstly, the control of active sites during the doping of metal elements is essential to ensure effective C–C coupling. This helps to avoid undesirable consequences such as oxidative deactivation of the photocatalyst due to insufficient V_O. Moreover, it is important to refrain from using reagent washing photocatalysts that affect the structure and catalytic performance of the photocatalysts. It is also worth noting that residual products remaining on the photocatalyst can influence the adsorption strength of CO_2 on its surface. Therefore, by refining the preparation methods of photocatalysts and enhancing the stability of their surface structures and properties during the compounding process, we can effectively improve the photocatalytic performance in CO_2-PR.

4.4. AQY

The activity of the CO_2-PR system is typically evaluated based on the rate of product generation or CO_2 conversion efficiency. However, normalizing the activity by unit photocatalyst mass (*i.e.*, $\mu mol\,h^{-1}\,g^{-1}$) is not appropriate since the reaction rate cannot be directly compared to the mass of the photocatalyst used. Additionally, it is not advisable to directly compare the reaction rates of photocatalysts reported by different research groups due to variations in experimental conditions. To effectively evaluate the activity of a specific photocatalyst, the measurement of the apparent quantum yield (AQY) in a reactive reduction process can be utilized.

In the work of Lu *et al.* [58], the effect of light irradiation on WO_{3-x}-2 was studied by obtaining the apparent quantum efficiency (AQE) of CO_2-PR under monochromatic light using different filters. The AQE estimates for monochromatic NIR-excitation and UV-excitation were found to be higher than that of monochromatic visible-NIR-excitation, indicating that the LSPR effect with energy band structure excitation enhances CO_2 conversion under UV–visible-NIR radiation. The AQE at 365 nm of the WO_{3-x}/MoO_{3-x} heterojunction, prepared by Liu *et al.* [101], is found to be 3.6 times higher than that of pure MoO_{3-x} and 2 times higher than that of pure WO_{3-x}. Abundant V_O formed in the WO_{3-x}/MoO_{3-x} heterojunction provide a large number of reduction sites for CO_2-PR, thereby enhancing the CO_2 adsorption and activation ability.

Currently, the highest reported AQY for W_xO_y-based photocatalysts is observed in the $WO_3/g\text{-}C_3N_4$ heterojunction in CO_2-PR applications. With 150 mg of $WO_3/g\text{-}C_3N_4$ under a light intensity of 20 mW/cm^2, the QY for CO_2-PR with H_2O at 40 °C was estimated as 3.829% for CH_4 and 0.733% for CO at an H_2O/CO_2 feed ratio of 0.40 [69]. These findings suggest that a higher H_2O/CO_2 feed ratio favors more CH_4 generation, while the RWGS reaction promotes CO generation under the same reaction conditions. The enhanced photoreactivity of $WO_3/g\text{-}C_3N_4$ heterojunctions for CO and CH_4 generation can be attributed to their larger exoactive surface area and more efficient carrier separation under visible light irradiation. Due to CO generation requires $2e^-$ while CH_4 requires $8e^-$, it is not possible to effectively analyze the photon flux utilization of CO_2-PR based solely on the generation rate. Therefore, it is more appropriate to calculate AQY when evaluating the performance of catalysts in different reaction systems.

5. Conclusion and perspective

Due to the growing interest in renewable resources, particularly solar energy, and the pressing need to convert increasing CO_2 greenhouse gas emissions into organic fuels, the exploration of W_xO_y-based materials has become a prominent area of research in CO_2-PR. This review paper aims to provide a comprehensive overview of the fundamental principles and products of CO_2-PR. Additionally, this paper examines various strategies that have been employed to enhance the photocatalytic efficiency of W_xO_y-based materials for CO_2-PR applications. While a significant body of research has demonstrated the promising potential of W_xO_y-based photocatalysts in CO_2-PR, there are still several challenges need to be addressed before their practical implementation. These challenges can be summarized into three main areas:

(1) W_xO_y-based photocatalysts continue to face challenges such as limited sunlight absorption and utilization efficiency, structural instability, carrier reorganization, and high redox capacity in the CO_2-PR process. Thus, it is essential to utilize the structural characteristics of W_xO_y which is abundant in V_O, enhance the role of active sites in promoting CO_2-PR process, fabricate additional heterojunctions to enhance both the efficiency and stability of W_xO_y-based materials in CO_2-PR.

(2) Another important aspect on W_xO_y-based photocatalysts is the selective production of high-value-added products. Currently, most W_xO_y-based photocatalysts for CO_2-PR primarily yield CO and CH_4 as products. The selective generation of high-value-added products through CO_2-PR poses a challenge. Hence, further attention should be directed towards studying W_xO_y-based materials and their role in promoting the generation of C2 products.

(3) Currently, the majority of studies evaluating the CO_2-PR activity primarily focus on the yield of products while often neglecting the carbon conversion efficiency. However, it should be noted that the reaction rate of CO_2-PR cannot be directly compared to the quality of the photocatalysts. Normalizing the activity to unit mass of the photocatalyst (*i.e.*, $\mu mol\,g^{-1}\,h^{-1}$) does not provide a proper assessment. As one of the essential factors for effectively assessing photocatalyst activity, calculating the CO_2 conversion efficiency allows us to visualize the catalytic performance exhibited by W_xO_y-based catalysts in CO_2-PR.

Declaration of competing interest

The authors declare that they have no known competing financial interests or personal relationships that could have appeared to influence the work reported in this paper.

CRediT authorship contribution statement

Weidan Meng: Writing – original draft. **Yanbo Zhou:** Methodology, Project administration, Supervision. **Yi Zhou:** Conceptualization, Project administration, Resources, Supervision, Validation, Writing – review & editing.

Acknowledgments

This work was supported by the National Natural Science Foundation of China (No. 22376065), the Science and Technology Commission of Shanghai Municipality (No. 22ZR1418600), Shanghai Municipal Science and Technology (No. 20DZ2250400).

Supplementary materials

Supplementary material associated with this article can be found, in the online version, at doi:10.1016/j.cclet.2024.109961.

References

[1] M.L. Ding, R.W. Flaig, H.L. Jiang, O.M. Yaghi, Chem. Soc. Rev. 48 (2019) 2783–2828.
[2] D. Voiry, H.S. Shin, K.P. Loh, M. Chhowalla, Nat. Rev. Chem. 2 (2018) 0105.
[3] C.T. Dinh, T. Burdyny, M.G. Kibria, et al., Science 360 (2018) 783–787.
[4] Y. He, M. Gao, Y. Zhou, Y. Zhou, Chemosphere 311 (2023) 136925.
[5] Y. Zhou, J. He, X. Li, J. Lu, Y. Zhou, Chem. Eng. J. 435 (2022) 132434.
[6] J. Lu, Q. Liu, Y. Zhang, Y. Zhou, Y. Zhou, Chin. Chem. Lett. 35 (2024) 109406.
[7] Y. Zhou, Y. He, M. Gao, et al., Chin. Chem. Lett. 35 (2024) 108690.
[8] F. Qin, E. Almatrafi, C. Zhang, et al., Angew. Chem. Int. Ed. 62 (2023) e202300256.
[9] S. Lan, C. Yu, F. Sun, et al., Nano Energy 93 (2022) 106792.
[10] J. He, X. Wang, S. Lan, et al., Appl. Catal. B: Environ. 317 (2022) 121747.
[11] D. Qin, Y. Zhou, W. Wang, et al., J. Mater. Chem. A 8 (2020) 19156–19195.
[12] J. Li, Z. Lou, B. Li, Chin. Chem. Lett. 33 (2022) 1154–1168.
[13] J. Huang, J. Wang, Z. Hao, et al., Chin. Chem. Lett. 32 (2021) 3180–3184.
[14] I. Hussain, A.A. Jalil, N.S. Hassan, M.Y.S. Hamid, J. Energy Chem. 62 (2021) 377–407.
[15] T.L. Wu, L. Liu, M.Y. Pi, D.K. Zhang, S.J. Chen, Appl. Surf. Sci. 377 (2016) 253–261.
[16] R.T. Guo, J. Wang, Z.X. Bi, et al., Chemosphere 295 (2022) 133834.
[17] K. Li, B.S. Peng, T.Y. Peng, ACS Catal. 6 (2016) 7485–7527.
[18] R. Zhai, L.H. Zhang, M.Y. Gu, et al., Small 19 (2023) 2207840.
[19] V.P. Indrakanti, J.D. Kubicki, H.H. Schobert, Energy Environ. Sci. 2 (2009) 745–758.
[20] L. Liu, W.L. Fan, X. Zhao, et al., Langmuir 28 (2012) 10415–10424.
[21] Z.F. Shen, Q.N. Xia, Y.G. Li, et al., J. CO_2 Util. 39 (2020) 101176.
[22] X.H. Feng, F.P. Pan, P. Zhang, et al., Chemphotochem 5 (2021) 79–89.
[23] L.M. Wang, W.L. Chen, D.D. Zhang, et al., Chem. Soc. Rev. 48 (2019) 5310–5349.
[24] H.A.E. Omr, M.W. Horn, H. Lee, Catalysts 11 (2021) 418.
[25] B. Wang, X.H. Wang, L. Lu, et al., ACS Catal. 8 (2018) 516–525.
[26] H.J. Yu, J.Y. Li, Y.H. Zhang, et al., Angew. Chem. Int. Ed. 58 (2019) 3880–3884.
[27] C.T. Campbell, C.H.F. Peden, Science 309 (2005) 713–714.
[28] H.J. Freund, M.W. Roberts, Surf. Sci. Rep. 25 (1996) 225–273.
[29] J. Raskó, Catal. Lett. 56 (1998) 11–15.
[30] Y.F. Ji, Y. Luo, J. Am. Chem. Soc. 138 (2016) 15896–15902.
[31] Y.Q. He, H. Rao, K.P. Song, et al., Adv. Funct. Mater. 29 (2019) 1905153.
[32] S.N. Habisreutinger, L. Schmidt-Mende, J.K. Stolarczyk, Angew. Chem. Int. Ed. 52 (2013) 7372–7408.
[33] K. Koci, L. Obalova, O. Solcova, Chem. Process Eng. 31 (2010) 395–407.
[34] Y.O. Wang, E.Q. Chen, J.W. Tang, ACS Catal. 12 (2022) 7300–7316.
[35] Y. He, Y. Zhou, J. Feng, M. Xing, Environ. Funct. Mater. 1 (2022) 204–217.
[36] K. Koci, L. Obalova, D. Placha, Z. Lacny, Collect. Czech. Chem. Commun. 73 (2008) 1192–1204.
[37] R. Das, S. Sarkar, R. Kumar, et al., ACS Catal. 12 (2021) 687–697.
[38] R.R. Ikreedeegh, M. Tahir, J. CO_2 Util. 43 (2021) 101381.
[39] N. Shehzad, M. Tahir, K. Johari, T. Murugesan, M. Hussain, J. CO_2 Util. 26 (2018) 98–122.
[40] G.C. Zuo, Y.T. Wang, W.L. Teo, Q.M. Xian, Y.L. Zhao, Appl. Catal. B: Environ. 291 (2021) 120126.
[41] P.G. Liu, Z.X. Huang, X.P. Gao, et al., Adv. Mater. 34 (2022) 2200057.
[42] Y. Ma, S. Wang, X. Duan, Chem. Eng. J. 455 (2023) 140654.
[43] A. Li, Q. Cao, G.Y. Zhou, et al., Angew. Chem. Int. Ed. 58 (2019) 14549–14555.
[44] J.F. Jing, J. Yang, W.L. Li, Z.H. Wu, Y.F. Zhu, Adv. Mater. 34 (2022) 2106807.
[45] Y.C. Hao, L.W. Chen, J. Li, et al., Nat. Commun. 12 (2021) 2682.
[46] Z.F. Huang, J. Song, X. Wang, et al., Nano Energy 40 (2017) 308–316.
[47] X.X. Guo, X.Y. Qin, Z.J. Xue, et al., RSC Adv. 6 (2016) 48537–48542.
[48] Y. Liu, Z. Zhang, Y. Fang, et al., Appl. Catal. B: Environ. 252 (2019) 164–173.
[49] X. Xie, Q.U. Hassan, H. Lu, et al., Chin. Chem. Lett. 32 (2021) 2038–2042.
[50] S. Sun, M. Watanabe, J. Wu, Q. An, T. Ishihara, J. Am. Chem. Soc. 140 (2018) 6474–6482.
[51] Y. Deng, J. Li, R. Zhang, et al., Chin. J. Catal. 43 (2022) 1230–1237.
[52] Y. Wang, R. Liu, M. Shi, et al., Chin. Chem. Lett. 34 (2023) 107200.
[53] N.N. Vu, S. Kaliaguine, T.O. Do, ChemSusChem 13 (2020) 3967–3991.
[54] D.B. Hemandez-Uresti, D. Sanchez-Martinez, A. Martinez-de la Cruz, S. Sepulveda-Guzman, L.M. Torres-Martinez, Ceram. Int. 40 (2014) 4767–4775.
[55] Y. Deng, Y. Liu, Y. Deng, et al., Chin. Chem. Lett. 35 (2024) 108898.
[56] J. Li, J. Feng, X. Guo, et al., Appl. Catal. B: Environ. 309 (2022) 121248.
[57] T. Li, X. Dong, W. Chen, et al., Appl. Surf. Sci. 526 (2020) 146578.
[58] C. Lu, J. Li, J. Yan, et al., Appl. Mater. Today 20 (2020) 100744.
[59] M. Shi, X. Tong, W. Li, et al., ACS Appl. Mater. Interface. 9 (2017) 34990–35000.
[60] Z. Xiong, Z. Lei, S. Ma, et al., Appl. Catal. B: Environ. 219 (2017) 412–424.
[61] Z. Zhu, X. Tang, T. Wang, et al., Appl. Catal. B: Environ. 241 (2019) 319–328.
[62] N. Ojha, A. Bajpai, S. Kumar, Catal. Sci. Technol. 9 (2019) 4598–4613.
[63] H. Wang, L. Zhang, K. Wang, X. Sun, W. Wang, Appl. Catal. B: Environ. 243 (2019) 771–779.
[64] M. Zhang, G. Cheng, Y. Wei, et al., J. Colloid Interface Sci. 572 (2020) 306–317.
[65] L. Yi, W. Zhao, Y. Huang, et al., Sci. China Mater. 63 (2020) 2206–2214.
[66] L. Wang, X.S. Zheng, L. Chen, Y.J. Xiong, H.X. Xu, Angew. Chem. Int. Ed. 57 (2018) 3454–3458.
[67] Y. Xiao, T. Wang, G.H. Qiu, et al., J. Colloid Interface Sci. 577 (2020) 459–470.
[68] S.B. Wang, B.Y. Guan, Y. Lu, X.W. Lou, J. Am. Chem. Soc. 139 (2017) 17305–17308.
[69] B. Tahir, M. Tahir, M.G.M. Nawawi, J. CO_2 Util. 41 (2020) 101270.
[70] X. Jiang, Y. Ding, S. Zheng, et al., ChemSusChem 15 (2022) e202102295.
[71] Z. Tang, C. Wang, W. He, et al., Chin. Chem. Lett. 33 (2022) 939–942.
[72] F. Xu, K. Meng, B. Cheng, et al., Nat. Commun. 11 (2020) 4613.
[73] A. Meng, B. Cheng, H. Tan, et al., Appl. Catal. B: Environ. 289 (2021) 120039.
[74] S. Karmakar, S. Barman, F.A. Rahimi, T.K. Maji, Energy Environ. Sci. 14 (2021) 2429–2440.

[75] X. Li, B. Kang, F. Dong, et al., Nano Energy 81 (2021) 105671.
[76] M. Lin, M. Luo, Y. Liu, et al., Chin. J. Catal. 50 (2023) 239–248.
[77] J. Wang, H. Cheng, D. Wei, Z. Li, Chin. J. Catal. 43 (2022) 2606–2614.
[78] Z. Xing, J. Hu, M. Ma, et al., J. Am. Chem. Soc. 141 (2019) 19715–19727.
[79] Y. Li, Y. Liu, D. Xing, et al., Appl. Catal. B: Environ. 285 (2021) 119855.
[80] H. Jiang, W. Wang, L. Sun, et al., J. Catal. 416 (2022) 1–10.
[81] L. Liang, X. Li, Y. Sun, et al., Joule 2 (2018) 1004–1016.
[82] Y. Huang, K. Dai, J. Zhang, G. Dawson, Chin. J. Catal. 43 (2022) 2539–2547.
[83] C. Zhu, X. Chen, J. Ma, et al., J. Phys. Chem. C 122 (2018) 20444–20458.
[84] X. Jiang, J. Huang, Z. Bi, et al., Adv. Mater. 34 (2022) 2109330.
[85] Y.J. Dong, Y. Jiang, J.F. Liao, et al., Sci. China Mater. 65 (2022) 1550–1559.
[86] Y.F. Li, N. Soheilnia, M. Greiner, et al., ACS Appl. Mater. Interfaces 11 (2019) 5610–5615.
[87] H. Zhang, Y. Wang, S. Zuo, et al., J. Am. Chem. Soc. 143 (2021) 2173–2177.
[88] Z. Zhu, W.R. Huang, C.Y. Chen, R.J. Wu, J. CO_2 Util. 28 (2018) 247–254.
[89] A. Raza, H. Shen, A.A. Haidry, et al., J. CO_2 Util. 37 (2020) 260–271.
[90] Q. Chen, X. Lan, K. Chen, Q. Ren, J. Shi, J. Colloid Interface Sci. 616 (2022) 253–260.
[91] P.Y. Jia, R.T. Guo, W.G. Pan, et al., Colloid Surface A 570 (2019) 306–316.
[92] Y. Feng, C. Wang, P. Cui, et al., Adv. Mater. 34 (2022) e2109074.
[93] L. Shen, Z. Xie, L. Hou, J. Yang, Q. Li, Energy Fuel. 36 (2022) 11515–11523.
[94] B. Weng, M.Y. Qi, C. Han, Z.R. Tang, Y.J. Xu, ACS Catal. 9 (2019) 4642–4687.
[95] C. Kuai, Z. Xu, C. Xi, et al., Nat. Catal. 3 (2020) 743–753.
[96] Z. Wan, G. Zhang, X. Wu, S. Yin, Appl. Catal. B: Environ. 207 (2017) 17–26.
[97] H. Dong, X. Guo, C. Yang, Z. Ouyang, Appl. Catal. B: Environ. 230 (2018) 65–76.
[98] G.F. Samu, C. Janáky, J. Am. Chem. Soc. 142 (2020) 21595–21614.
[99] D. Zeng, H. Wang, X. Zhu, et al., Chem. Eng. J. 451 (2023) 138801.
[100] W. Shi, X. Guo, C. Cui, et al., Appl. Catal. B: Environ. 243 (2019) 236–242.
[101] Y. Liu, X. Dong, Q. Yuan, et al., Colloid Surface A 621 (2021) 126582.